nature materials

ARTICLES

PUBLISHED ONLINE: 5 OCTOBER 2015 | DOI: 10.1038/NMAT4430

Convergence of multi-valley bands as the electronic origin of high thermoelectric performance in $CoSb_3$ skutterudites

Yinglu Tang[1,2†], Zachary M. Gibbs[3†], Luis A. Agapito[4,5], Guodong Li[1,2,6], Hyun-Sik Kim[1,2,7], Marco Buongiorno Nardelli[4], Stefano Curtarolo[5] and G. Jeffrey Snyder[1,2*]

Filled skutterudites $R_xCo_4Sb_{12}$ are excellent n-type thermoelectric materials owing to their high electronic mobility and high effective mass, combined with low thermal conductivity associated with the addition of filler atoms into the void site. The favourable electronic band structure in n-type $CoSb_3$ is typically attributed to threefold degeneracy at the conduction band minimum accompanied by linear band behaviour at higher carrier concentrations, which is thought to be related to the increase in effective mass as the doping level increases. Using combined experimental and computational studies, we show instead that a secondary conduction band with 12 conducting carrier pockets (which converges with the primary band at high temperatures) is responsible for the extraordinary thermoelectric performance of n-type $CoSb_3$ skutterudites. A theoretical explanation is also provided as to why the linear (or Kane-type) band feature is not beneficial for thermoelectrics.

With the world's increasing demand for energy, there is an imminent need for sustainable power-generation solutions including solar, wind, or geothermal. Thermoelectric materials can help increase the energy efficiency of fuels by converting waste heat, such as that of automobile exhausts, directly into electricity using no moving parts. The maximum efficiency of thermoelectric materials is characterized by the dimensionless figure of merit, $zT = S^2\sigma T/\kappa$, where S is the Seebeck coefficient, σ is the electrical conductivity, T is the absolute temperature, and κ is the total thermal conductivity.

Among the best thermoelectric materials are n-type filled skutterudites based on $CoSb_3$. The addition of filler atoms, for example Yb, into a void site ($Yb_xCo_4Sb_{12}$) can lead to high zT by reducing the thermal conductivity while simultaneously doping the material (adding electrons as charge carriers)[1,2]. High zT values (greater than 1) have been reported for both single-element filling (Na (ref. 3), Ba (ref. 4), In (ref. 5), Ce (ref. 6), and so on) and multiple filling (In+Ce (ref. 7), Sr+Ba+Yb (ref. 8), Ba+La+Yb (ref. 9)). High zT in skutterudites is most often attributed to the addition of the filler atoms and subsequent reduction in thermal conductivity due to alloying disorder and the complex phonon modes of the filler atom[10–12].

Although low thermal conductivity is essential to high zT, the importance of the intrinsic electronic structure in skutterudites is often understated or ignored completely. It has become increasingly apparent that complex band structures—including multi-valley Fermi surfaces[13,14], convergence of bands (PbTe (ref. 14), PbSe (ref. 15), Mg_2Si (ref. 16)), or even threads of Fermi-surface-connecting band extrema[17]—are key features of many good thermoelectric materials because the thermoelectric quality factor, B, is proportional to N_v (refs 13,18), the number of degenerate valleys in the electronic structure (or pockets of Fermi surface). Whereas most common semiconductors or metals have simple Fermi surfaces with one or three pockets, thermoelectric materials with $zT > 1$ often have $N_v = 6$ or more[13,15].

$CoSb_3$ is known to have very light bands, making a very small (0.05–0.22 eV) direct bandgap[19,20]. The single, light valence band has an approximately linear ($E \sim k$ rather than the usual parabolic $E = \hbar^2k^2/2m^*$) dispersion. The light effective mass explains the high mobility observed in lightly doped p-type $CoSb_3$ (ref. 1) and is beneficial to zT (ref. 21), but it also makes the thermopower (magnitude of the Seebeck coefficient) decrease more quickly as the material is doped. The conduction bands in n-type $CoSb_3$ skutterudites are also very light, with one of the three bands mirroring the linear valence band. The n-type thermopower, however, remains high at high doping, where the linear band concept has been used to explain the apparent increase in effective mass[1,22–25]. This high thermopower at high doping is essential to achieve the high zT in all n-type skutterudites. Here we show that this essential feature of the electronic structure cannot be due to the linear band, but instead is due to a new band (or bands) with high valley degeneracy of $N_v = 12$ or more.

Results and discussion

Multiple conduction band behaviour in n-type $CoSb_3$. Here we shall describe the transport properties of $Yb_xCo_4Sb_{12}$ using a rigid band approximation[26,27], meaning that the conduction band structure does not change significantly with doping

[1]Department of Materials Science and Engineering, Northwestern University, Evanston, Illinois 60208, USA. [2]Materials Science, California Institute of Technology, Pasadena, California 91125, USA. [3]Division of Chemistry and Chemical Engineering, California Institute of Technology, Pasadena, California 91125, USA. [4]Department of Physics, University of North Texas, Denton, Texas 76203, USA. [5]Department of Mechanical Engineering and Materials Science, Physics and Chemistry, Duke University, Durham, North Carolina 27708, USA. [6]State Key Laboratory of Advanced Technology for Materials Synthesis and Processing, Wuhan University of Technology, Wuhan, Hubei 430070, China. [7]Materials Research Center, Samsung Advanced Institute of Technology, Samsung Electronics, Suwon 443-803, South Korea. †These authors contributed equally to this work.
*e-mail: jeff.snyder@northwestern.edu

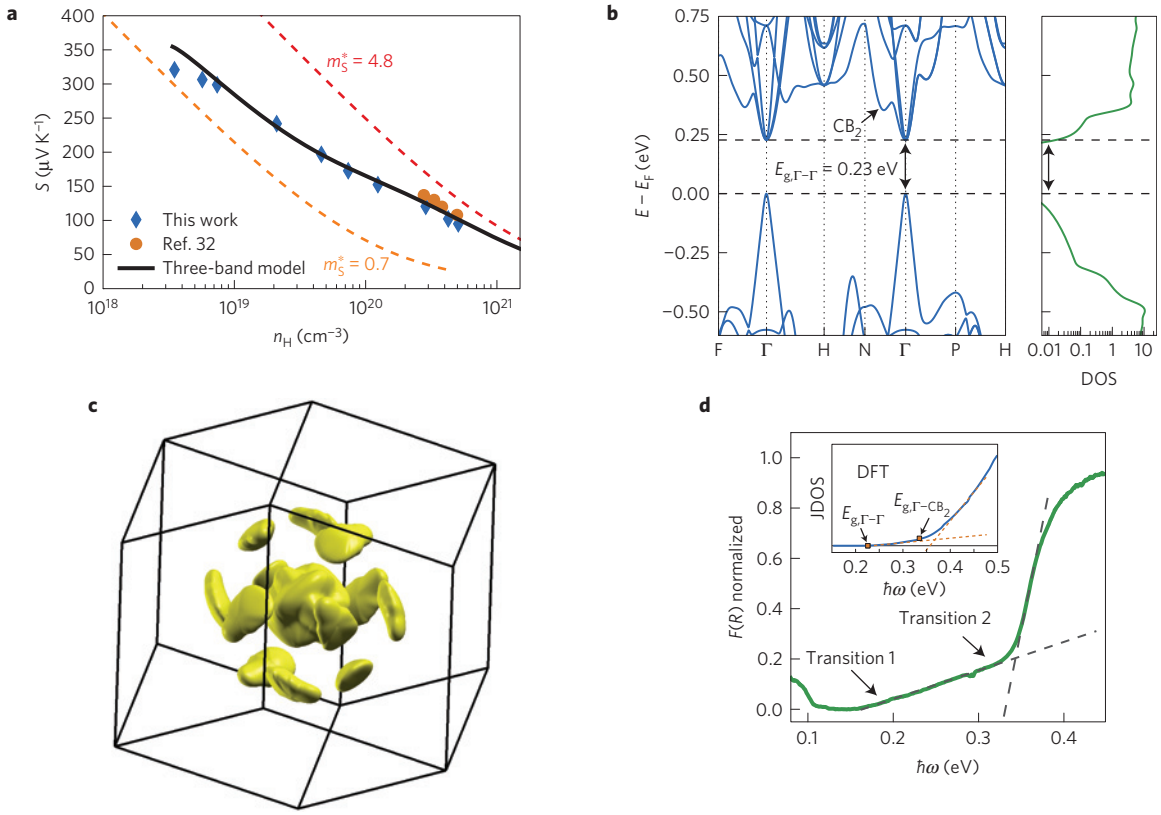

Figure 1 | Experimental and theoretical evidence showing multiple conduction bands in n-type $CoSb_3$. a, Pisarenko plot of Seebeck coefficient (S) versus Hall carrier concentration (n_H) at 300 K. The solid black line (three-band model) represents the prediction of a semi-empirical model with two conduction bands plus one valence band as described in the Supplementary Information, Section 4. Orange and red dashed lines show the expected S versus n_H behaviour for single parabolic bands with masses equal to the two individual conduction bands. The data of ref. 32 on Yb-filled $CoSb_3$ are included for comparison. **b**, DFT-calculated electronic band structure and density of states (DOS) for $CoSb_3$. **c**, Fermi surface calculation for a Fermi level 0.11 eV above the conduction band minimum showing the 12 pockets of the second conduction band CB_2 observed as a valley between Γ–N. **d**, Room-temperature optical absorption measurement with the estimated joint density of states from DFT showing two distinct transitions.

(Yb content) from that of unfilled $CoSb_3$. Experimentally, similar electronic properties are obtained whether $CoSb_3$ is doped through filling or by substitution on the Co or Sb sites[1,22,24,25] (with optimum thermoelectric performance of the order of 10^{20} cm^{-3} or 0.5 electrons per unit cell)[9,27], in accordance with the rigid band model. Filled $Yb_xCo_4Sb_{12}$ is shown theoretically to be essentially rigid band up to $x = 0.25$ (0.5 electrons per unit cell[27]). In other thermoelectric materials, such as PbTe, rigid band models have been used successfully and have been confirmed theoretically[28].

Multiple band effects that are responsible for the exceptionally high zT in n-type $CoSb_3$ are observable through several methods, both experimental and theoretical, as presented in Fig. 1. A clear demonstration of complex band behaviour is seen in the doping-dependent Seebeck coefficient (Pisarenko plot at 300 K) shown in Fig. 1a. In the degenerate limit the relationship between S, m_S^* and n can be described by:

$$S = \frac{2k_B^2 T}{3e\hbar^2}\left(\frac{\pi}{3n}\right)^{\frac{2}{3}} m_S^*(1+r) \qquad (1)$$

where e is the electron charge, k_B is the Boltzmann constant, $\hbar$ is the reduced Planck constant, r is the scattering parameter ($r = 0$ for acoustic phonon scattering, which is fairly common above 300 K and is most appropriate for $CoSb_3$), and m_S^* is the density of states (DOS) effective mass obtained from Seebeck measurements using the single parabolic band (SPB) model (which will be referred to as the Seebeck mass herein). At low carrier concentrations (n_H less than $\sim 1 \times 10^{19}$ cm^{-3}), $CoSb_3$ shows light mass behaviour ($m_S^* \sim 0.7\, m_e$); as the carrier concentration increases, the system transitions to a much heavier mass, requiring $m_S^* = 4.8\, m_e$ in the heavily doped regime (n_H larger than 3×10^{20} cm^{-3}). By considering two conduction bands[29–31] plus one valence band in a three-band transport model (with a conduction band offset ΔE of $\sim$0.08 eV), we capture the behaviour of both the lightly and the heavily doped regions (black line in Fig. 1a).

The calculated electronic band structure is consistent with an increasing m_S^*, that becomes gradually heavier with doping, if we consider not only the primary conduction bands (Γ point), but also the bands higher in energy (labelled CB_2 in Fig. 1b) for heavily doped $CoSb_3$. The *ab initio* density functional theory (DFT) calculated band structure (Fig. 1b) shows a direct bandgap at the Γ point ($E_{g,\Gamma-\Gamma} = 0.23$ eV), which yields a triply degenerate ($N_v = 3$) conduction band edge. However, as a result of heavy doping and relatively light bands at the conduction band minimum, the Fermi level quickly moves up the conduction band, allowing a large population of electrons to form in the secondary conduction band (CB_2). Calculations show that this CB_2 minimum exists about 0.11 eV above the conduction band minimum along Γ–N, and that the Fermi level (E_F) should be well within CB_2 with 0.5 electrons/unit cell[27,33] (E_F reaches the CB_2 minimum with $n_H \approx 2 \times 10^{20}$ cm^{-3} at $T = 300$ K). The iso-energy Fermi surface for an energy level just at CB_2 (Fig. 1c) has a high degeneracy with 12 isolated pockets[33]. Only PbTe, which reaches a zT of $\sim$2 (ref. 13), has such a high value of N_v; it has been shown that this high N_v plays a crucial role in the high Seebeck values and zT. In $CoSb_3$, at higher energies these 12 pockets join at corners along Γ–F ($N_v = 24$, 0.013 eV above CB_2; ref. 33) and then to the Γ Fermi surface

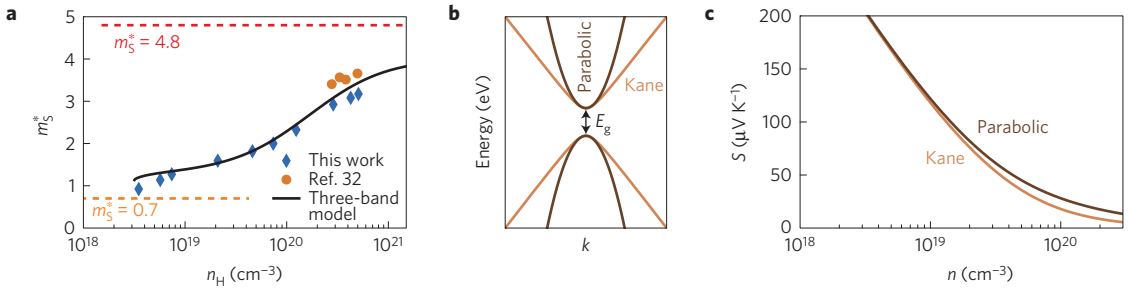

Figure 2 | Band non-parabolicity and its effect on the Seebeck coefficient and energy-dependent Seebeck effective mass, $m_S^*(E)$. **a**, Effective mass $m_S^*(E)$ derived from Seebeck coefficient and Hall effect measurements. The solid black line (three-band model) represents the prediction of a semi-empirical model with two conduction bands plus one valence band (as detailed in the Supplementary Information, Section 4). Orange and red dashed lines indicate the band masses of the two individual conduction bands. The data of ref. 32 is included for comparison. **b**, Parabolic and Kane band dispersions with the same band-edge effective mass ($m_S^*(E=0)$). **c**, Seebeck Pisarenko plot for both Kane and Parabolic bands, illustrating that $m_S^*(E)$ actually decreases for Kane bands at high carrier concentration.

before closing up an opening at Γ–H ($N_v = 6$, 0.034 eV above CB_2). Supplementary Fig. 5 shows these Fermi surfaces in greater detail in the Supplementary Information, Section 6.

In addition to thermoelectric transport and DFT calculations, multi-band features in $CoSb_3$ can be directly observed by infrared (IR) optical absorption. Optical absorption edge spectra for a nearly intrinsic sample of $CoSb_3$ ($n_H = 1.7 \times 10^{17}$ cm^{-3}) show two distinct features (Fig. 1d). The lower-energy (~0.2 eV optically, 0.23 eV from DFT) transition can be associated with the direct, Γ–Γ transition, and the second transition (~0.3 eV optically, 0.34 eV from DFT) indicates the onset of a Γ–CB_2 transition. Although direct transitions have been shown to exhibit more than ten times the strength of absorption of the indirect transitions[34], the transition rate is also proportional to the DOS. Because both VB_Γ and CB_Γ have very low DOS in comparison to CB_2, the Γ–Γ transition, despite the fact that it is a direct transition, may occur with a lower intensity than the Γ–CB_2 transition. We roughly estimate the strength of all transitions by calculating the joint density of states (JDOS) from the DFT band structure in the inset of Fig. 1d, which weights both direct and indirect transitions equally. The JDOS agrees with the observation of two slopes from the optical data. Historically, optical measurements in the skutterudite system have been limited, showing an optical band gap for CoP_3 of 0.45 eV; no optical gap had been found for $CoSb_3$ or $CoAs_3$ (see the Supplementary Information, Section 3 for additional details)[35]. This was probably because the lowest photon energy that they had measured was 0.4 eV. Other optical measurements have focused on very low energies (<0.1 eV) to probe optical phonons[36], just missing the frequency range important for interband transitions.

Linear or Kane bands do not increase Seebeck mass. The unexpectedly high thermopower at high carrier density in $Yb_xCo_4Sb_{12}$ observed in the Pisarenko plot of Fig. 1a can also be represented as an increase in m_S^*, the Seebeck effective mass, as a function of carrier concentration, as shown in Fig. 2a. This apparent increase in effective mass with doping has previously been attributed to non-parabolic (Kane) bands[1,22–25], rather than multi-band effects. A non-parabolic dispersion (shown in Fig. 2b; equation (2)) can arise as a result of interaction between the valence and conduction bands, common in narrow gap semiconductors, which can be described using $k \cdot p$ perturbation theory[37]. Such bands are often described by a dispersion relation where the band is approximately parabolic near the band edge (at $E = 0$, with band-edge effective mass m_0^*), but they become more linear as the electron energy, E, becomes large relative to the bandgap E_g.

$$E\left(1+\frac{E}{E_g}\right)=\frac{\hbar^2k^2}{2m_0^*} \tag{2}$$

where k is the electron wavevector. For non-parabolic bands, effective mass is not well defined because there are different definitions for m^*, based on different classical relationships. In non-parabolic transport theory, the commonly used energy-dependent effective mass derived from the electron momentum is:

$$m_p^*(E)=\hbar^2k\left(\frac{dE}{dk}\right)^{-1}=m_0^*\left(1+\frac{2E}{E_g}\right) \tag{3}$$

This is a different definition than that found in most solid state physics textbooks, $m^* = \hbar^2(d^2E/dk^2)^{-1}$, which relates the effective mass to the band curvature directly. Many common semiconducting materials are reported to show $m^*(E)$ increasing with energy (Fermi level, E_F), including InSb (ref. 38), InAs (ref. 39), GaAs (ref. 39), PbTe (ref. 40) and others in a variety of different measurements, including electrical susceptibility (measured using optical reflectance)[40,41], Shubnikov–De Haas/De Haas–Van Alphen oscillations[42], Faraday rotation[38,39], and combined galvano thermomagnetic measurements (Seebeck and Nernst coefficients)[43]. In general these measurements are analysed based on the dispersion relation equation (2) to derive the $m_p^*(E)$ of equation (3). However, we will show that such an increasing trend with energy should not be expected on the Seebeck Pisarenko plot, and instead a decrease in Seebeck mass $m_S^*(E)$ is predicted in the case of a non-parabolic band with a dispersion given by equation (2).

For thermoelectric materials we define the Seebeck mass $m_S^*(E)$ as the DOS effective mass that would give the measured Seebeck coefficient with the measured n_H using a SPB model[1] (that is, equation (1) in the degenerate limit). In $CoSb_3$, this carrier-concentration-dependent DOS effective mass $m_S^*(E)$ is observed to increase with n_H in both n-type (Fig. 2a) and p-type materials; this increase is commonly attributed to band non-parabolicity using equations (2) and (3) (refs 1,22–25,42). However, we must realize that these two distinct definitions of effective mass, $m_S^*(E)$ and $m_p^*(E)$, are qualitatively different. For example, the degenerate limit of the Seebeck coefficient with a Kane dispersion relation (the equation analogous to equation (1) using the Kane dispersion, equation (2)) can be expressed as[44]:

$$S=\frac{2k_B^2T}{3e\hbar^2}\left(\frac{\pi}{3n}\right)^{\frac{2}{3}}m_p^*(E)(1+r-\lambda) \tag{4}$$

where an additional correction factor

$$\lambda=\frac{\frac{4E}{E_g}\left(1+\frac{E}{E_g}\right)}{\left(1+\frac{2E}{E_g}\right)^2}$$

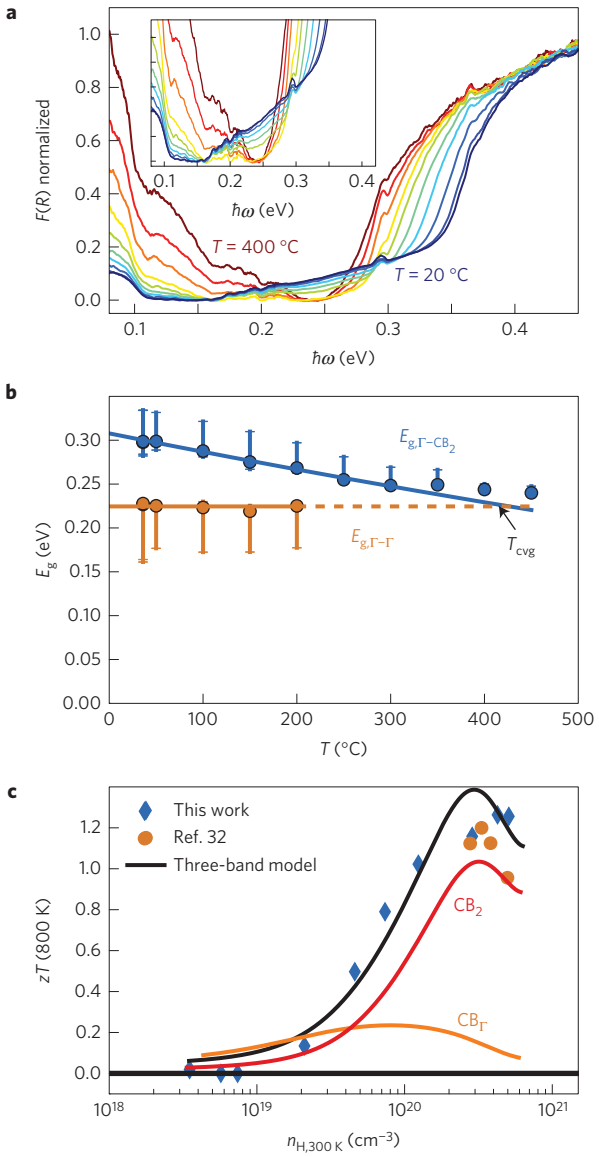

Figure 3 | High-temperature band convergence in $CoSb_3$ as shown from optical absorption and thermoelectric figure of merit. **a**, Temperature-dependent optical absorption for $CoSb_3$ from 20 to 400 °C. **b**, Temperature-dependent bandgap for the direct ($E_{g,\Gamma-\Gamma}$) and indirect ($E_{g,\Gamma-CB_2}$) transitions indicating band convergence at 800 ± 100 K. Error bars represent the range of extrapolations obtained for both the primary and secondary transitions (as detailed in the Methods and Supplementary Information, Section 3). **c**, zT at 800 K versus carrier concentration n_H measured at 300 K compared with that predicted with the model (solid black line). Coloured lines labelled CB_Γ and CB_2 represent the zT that could have been attained by the primary and secondary conduction bands respectively with the valence band (as detailed in the Methods and Supplementary Information, Section 4). Ref. 32 shows the measured zT for comparison[32].

has been added to the equation for that of a parabolic band (equation (1)). Thus, m_S^*, as used in thermoelectric studies, does not necessarily increase with doping or Fermi level as the momentum mass does. In fact, when $r = 0$, as is commonly found in thermoelectric materials, the m_S^* mass in a Kane band should actually decrease according to:

$$m_S^*(E) = \frac{m_0^*}{1 + \frac{2E}{E_g}} \quad (5)$$

which is derived by substituting the expression for λ into equation (4) and comparing the result with the SPB result (equation (1)). Additional details regarding this derivation are included in the Supplementary Information, Section 5. The effect of this relation can be seen in Fig. 2c, which shows a Seebeck coefficient that is lower for the Kane band ($m_S^*(E)$ decreased).

In other words, even though $m_P^*(E)$ increases with energy in a Kane band, the Seebeck coefficient and $m_S^*(E)$ should actually decrease relative to that of a parabolic band, as shown in Fig. 2c. This may be surprising because both $m_P^*(E)$ and $m_S^*(E)$ are described as a density of states effective mass and often implicitly expected to exhibit the same trends. Instead, equation (5) shows that the Kane band dispersion, and linear bands in general, do not increase $m_S^*(E)$ or benefit thermoelectric performance relative to a parabolic band with the same band-edge effective mass. For $CoSb_3$, equation (5) demonstrates that the increasing m_S^* in Fig. 2a is not evidence of Kane-type behaviour, but rather that multiple conduction bands are necessary to explain the properties of $CoSb_3$.

Band convergence at high temperatures. We have shown that a second band is required to explain the room-temperature transport and optical properties. However, it is at high temperatures where the thermoelectric performance of $CoSb_3$ excels. At high temperatures, we show that these exceptional properties are probably the result of band convergence, as indicated by optical absorption edge measurements that show the two conduction bands approach each other, leading to convergence at $T_{cvg} \approx 800 \pm 100$ K (with effective convergence, that is, $\Delta E < 1k_BT$, for $T > 500$ K). This band convergence further increases the effective valley degeneracy to $N_v \approx 12$–15. The optical absorption measured from 20–450 °C clearly shows that the strong Γ–CB_2 absorption decreases in onset energy with temperature (Fig. 3a). The extrapolated absorption edges (Fig. 3b) indicate that the primary (Γ–Γ, direct) transition does not shift much with temperature (and actually is overtaken by free carrier absorption at high temperatures), whereas the secondary band (Γ–CB_2) shows a clear temperature-dependent decrease in energy at a rate of $\sim -2.0 \times 10^{-4}$ eV K^{-1}. As the two bands become closer in energy, both bands will contribute significantly to thermoelectric transport and improve the thermoelectric quality factor and zT in the same way that band convergence enables high zT in p-type PbTe (ref. 13).

The high zT in $Yb_xCo_4Sb_{12}$ can now be shown to be a direct result of the high valley degeneracy inherent to $CoSb_3$, which is further enhanced by band convergence at high temperatures. Figure 3c shows the carrier-concentration-dependent zT for a series of Yb-doped samples at 800 K along with the calculated results of a three-band model (two conduction bands and one valence band, with details given in the Methods and Supplementary Information, Section 4). From this plot, we can see the benefits that having a second conduction band allows, resulting in a significantly higher zT than the primary conduction band at Γ can provide alone. If we consider both the primary (CB_Γ, $N_v = 3$) and the secondary band (CB_2, $N_v = 12$) in the context of band engineering and the quality factor:

$$B = \frac{2k_B^2\hbar}{3\pi} \frac{N_v C_L}{m_c^* E_{def}^2 \kappa_L} T$$

($m_\Gamma^* \approx 0.42$, $m_{CB_2}^* \approx 2.88$ at 800 K), we determine that B_{CB_2} is about four times that of B_Γ (as indicated by the much larger maximum zT in Fig. 3 at 800 K). Because CB_Γ and CB_2 are very near converged at high temperatures ($\Delta E \approx 0$ for 800 K), the overall quality factor is enhanced by the presence of the second band, as both bands can be thought to conduct in parallel, thereby increasing the electrical conductivity without being detrimental to the Seebeck coefficient (in the limit of converged bands $B_{total} = B_{CB_\Gamma} + B_{CB_2}$ (ref. 45)). Thus both bands contribute to the high thermoelectric performance.

A unified picture explaining the extraordinary thermoelectric properties of skutterudites has emerged from a combined analysis of transport measurements, optical absorption, and theory on a series of $Yb_xCo_4Sb_{12}$ samples. The primary light conduction bands at Γ have a reasonable thermoelectric quality factor, but they are significantly aided by a secondary conduction band, which has extremely high valley degeneracy $N_v = 12$. At high temperatures these two bands converge, enabling the extraordinarily high $zT > 1$ that is observed in many $CoSb_3$-based skutterudites with a variety of filling and doping elements. The contribution of band convergence to the performance at high temperatures suggests that band engineering methods[18] to converge the two conduction bands at lower temperatures would improve the low-temperature zT. The analysis of linear and Kane bands presented here suggests that non-parabolic band dispersions do not lead to an increase in thermopower (Seebeck coefficient) and are not beneficial to thermoelectric performance.

Methods

Methods and any associated references are available in the online version of the paper.

Received 1 June 2015; accepted 25 August 2015; published online 5 October 2015

References

1. Caillat, T., Borshchevsky, A. & Fleurial, J. P. Properties of single crystalline semiconducting $CoSb_3$. *J. Appl. Phys.* **80,** 4442–4449 (1996).
2. Tang, Y., Chen, S. W. & Snyder, G. J. Temperature dependent solubility of Yb in Yb–$CoSb_3$ skutterudite and its effect on preparation, optimization and lifetime of thermoelectrics. *J. Materiom.* **1,** 75–84 (2015).
3. Pei, Y. Z. *et al.* Improving thermoelectric performance of caged compounds through light-element filling. *Appl. Phys. Lett.* **95,** 042101 (2009).
4. Chen, L. D. *et al.* Anomalous barium filling fraction and n-type thermoelectric performance of $Ba_yCo_4Sb_{12}$. *J. Appl. Phys.* **90,** 1864–1868 (2001).
5. Tang, Y. *et al.* Phase diagram of In–Co–Sb system and thermoelectric properties of In-containing skutterudites. *Energy Environ. Sci.* **7,** 812–819 (2014).
6. Tang, Y., Hanus, R., Chen, S. W. & Snyder, G. J. Solubility design leading to high figure of merit in low-cost Ce–$CoSb_3$ skutterudites. *Nature Commun.* **6,** 7584 (2015).
7. Li, H., Tang, X., Zhang, Q. & Uher, C. High performance $In_xCe_yCo_4Sb_{12}$ thermoelectric materials with *in situ* forming nanostructured InSb phase. *Appl. Phys. Lett.* **94,** 102114 (2009).
8. Rogl, G. *et al.* n-type skutterudites $(R,Ba,Yb)_yCo_4Sb_{12}$ (R = Sr, La, Mm, DD, SrMm, SrDD) approaching ZT ≈ 2.0. *Acta Mater.* **63,** 30–43 (2014).
9. Shi, X. *et al.* Multiple-filled skutterudites: High thermoelectric figure of merit through separately optimizing electrical and thermal transports. *J. Am. Chem. Soc.* **133,** 7837–7846 (2011).
10. Meisner, G., Morelli, D., Hu, S., Yang, J. & Uher, C. Structure and lattice thermal conductivity of fractionally filled skutterudites: Solid solutions of fully filled and unfilled end members. *Phys. Rev. Lett.* **80,** 3551–3554 (1998).
11. Koza, M. M. *et al.* Breakdown of phonon glass paradigm in La- and Ce-filled Fe_4Sb_{12} skutterudites. *Nature Mater.* **7,** 805–810 (2008).
12. Nolas, G. S., Fowler, G. & Yang, J. Assessing the role of filler atoms on the thermal conductivity of filled skutterudites. *J. Appl. Phys.* **100,** 043705 (2006).
13. Pei, Y. *et al.* Convergence of electronic bands for high performance bulk thermoelectrics. *Nature* **473,** 66–69 (2011).
14. Zhao, L. D. *et al.* All-scale hierarchical thermoelectrics: MgTe in PbTe facilitates valence band convergence and suppresses bipolar thermal transport for high performance. *Energy Environ. Sci.* **6,** 3346–3355 (2013).
15. Wang, H., Gibbs, Z. M., Takagiwa, Y. & Snyder, G. J. Tuning bands of PbSe for better thermoelectric efficiency. *Energy Environ. Sci.* **7,** 804–811 (2014).
16. Liu, W. *et al.* Convergence of conduction bands as a means of enhancing thermoelectric performance of n-type $Mg_2Si_{1-x}Sn_x$ solid solutions. *Phys. Rev. Lett.* **108,** 166601 (2012).
17. Parker, D., Chen, X. & Singh, D. J. High three-dimensional thermoelectric performance from low-dimensional bands. *Phys. Rev. Lett.* **110,** 146601 (2013).
18. Pei, Y., Wang, H. & Snyder, G. J. Band engineering of thermoelectric materials. *Adv. Mater.* **24,** 6125–6135 (2012).
19. Singh, D. J. & Pickett, W. E. Skutterudite antimonides: Quasilinear bands and unusual transport. *Phys. Rev. B* **50,** 11235–11238 (1994).
20. Sofo, J. O. & Mahan, G. D. Electronic structure of $CoSb_3$: A narrow-band-gap semiconductor. *Phys. Rev. B* **58,** 15620–15623 (1998).
21. Pei, Y., LaLonde, A. D., Wang, H. & Snyder, G. J. Low effective mass leading to high thermoelectric performance. *Energy Environ. Sci.* **5,** 7963–7969 (2012).
22. Kuznetsov, V. L., Kuznetsova, L. A. & Rowe, D. M. Effect of partial void filling on the transport properties of $Nd_xCo_4Sb_{12}$ skutterudites. *J. Phys. Condens. Matter* **15,** 5035–5048 (2003).
23. Salvador, J. R., Yang, J., Wang, H. & Shi, X. Double-filled skutterudites of the type $Yb_xCa_yCo_4Sb_{12}$: Synthesis and properties. *J. Appl. Phys.* **107,** 043705 (2010).
24. Anno, H., Matsubara, K., Notohara, Y., Sakakibara, T. & Tashiro, H. Effects of doping on the transport properties of $CoSb_3$. *J. Appl. Phys.* **86,** 3780–3786 (1999).
25. Dyck, J. S. *et al.* Thermoelectric properties of the n-type filled skutterudite $Ba_{0.3}Co_4Sb_{12}$ doped with Ni. *J. Appl. Phys.* **91,** 3698–3705 (2002).
26. Zhou, A., Liu, L.-S., Zhai, P.-C., Zhao, W.-Y. & Zhang, Q.-J. Electronic structures and transport properties of single-filled $CoSb_3$. *J. Electron. Mater.* **39,** 1832–1836 (2010).
27. Yang, J., Xi, L., Zhang, W., Chen, L. D. & Yang, J. Electrical transport properties of filled $CoSb_3$ skutterudites: A theoretical study. *J. Electron. Mater.* **38,** 1397–1401 (2009).
28. Takagiwa, Y., Pei, Y. Z., Pomrehn, G. & Snyder, G. J. Validity of rigid band approximation of PbTe thermoelectric materials. *Appl. Phys. Lett. Mater.* **1,** 011101 (2013).
29. Liu, W-S., Zhao, L-D., Zhang, B-P., Zhang, H.-L. & Li, J.-F. Enhanced thermoelectric property originating from additional carrier pocket in skutterudite compounds. *Appl. Phys. Lett.* **93,** 042109 (2008).
30. Nagamoto, Y., Tanaka, K. & Koyanagi, T. *Thermoelectrics, 1998. Proceedings ICT 98. XVII International Conference on* 302–305 (IEEE, 1998).
31. Kajikawa, Y. Refined analysis of the transport properties of $Co_{1-x}Ni_xSb_3$ according to a model including a deep donor level and the second lowest valleys of the conduction band. *J. Alloys Compd.* **621,** 170–178 (2015).
32. Yang, J. *et al.* Solubility study of Yb in n-type skutterudites $Yb_xCo_4Sb_{12}$ and their enhanced thermoelectric properties. *Phys. Rev. B* **80,** 115329 (2009).
33. Chaput, L., Pécheur, P., Tobola, J. & Scherrer, H. Transport in doped skutterudites: *Ab initio* electronic structure calculations. *Phys. Rev. B* **72,** 085126 (2005).
34. Gnutzman, U. & Clauseck, K. Theory of direct optical-transitions in an optical indirect semiconductor with a superlattice structure. *Appl. Phys.* **3,** 9–14 (1974).
35. Ackermann, J. & Wold, A. The preparation and characterization of the cobalt skutterudites CoP_3, $CoAs_3$ and $CoSb_3$. *J. Phys. Chem. Solids* **38,** 1013–1016 (1977).
36. Kliche, G. & Lutz, H. D. Temperature dependence of the FIR reflection spectra of the skutterudites $CoAs_3$ and $CoSb_3$. *Infrared Phys.* **24,** 171–177 (1984).
37. Kane, E. O. Band structure of indium antimonide. *J. Phys. Chem. Solids* **1,** 249–261 (1957).
38. Smith, S. D., Moss, T. S. & Taylor, K. W. The energy-dependence of electron mass in indium antimonide determined from measurements of the infrared Faraday effect. *J. Phys. Chem. Solids* **11,** 131–139 (1959).
39. Cardona, M. Electron effective masses of InAs and GaAs as a function of temperature and doping. *Phys. Rev.* **121,** 752–758 (1961).
40. Dixon, J. R. & Riedl, H. R. Electric-susceptibility hole mass of lead telluride. *Phys. Rev.* **138,** A873–A881 (1965).
41. Dionne, G. & Woolley, J. C. Optical properties of some $Pb_{1-x}Sn_xTe$ alloys determined from infrared plasma reflectivity measurements. *Phys. Rev. B* **6,** 3898–3913 (1972).
42. Arushanov, E., Respaud, M., Rakoto, H., Broto, J. M. & Caillat, T. Shubnikov–de Haas oscillations in $CoSb_3$ single crystals. *Phys. Rev. B* **61,** 4672–4676 (2000).
43. Harman, T. C. Galvano-thermomagnetic effects in semiconductors and semimetals—IV. mercury selenide. *J. Phys. Chem. Solids* **25,** 931–940 (1964).
44. Young, D. L., Coutts, T. J., Kaydanov, V. I., Gilmore, A. S. & Mulligan, W. P. Direct measurement of density-of-states effective mass and scattering parameter in transparent conducting oxides using second-order transport phenomena. *J. Vac. Sci. Technol. A* **18,** 2978–2985 (2000).
45. Pshenaï-Severin, D. A. & Fedorov, M. I. Effect of the band structure on the thermoelectric properties of a semiconductor. *Phys. Solid State* **49,** 1633–1637 (2007).

Acknowledgements

We acknowledge the funding support of the Materials Project by Department of Energy Basic Energy Sciences Program under Grant No. EDCBEE, DOE Contract DE-AC02-05CH11231 (DFT band structure calculation, Fermi surface plot, optical measurements, modelling); DOE-Gentherm (sample synthesis, structural characterization and thermoelectric property measurements); Solid-State Solar-Thermal Energy Conversion Center (S3TEC), an Energy Frontier Research Center funded by the US Department of Energy, Office of Science, Basic Energy Sciences under Award #DE-SC0001299 (modelling, preparation of the manuscript). L.A., M.B.N. and S.C. acknowledge the support of the DOD (ONR-MURI under Contract N00014-13-1-0635). The band structure analysis for this project was mainly performed at Texas Advanced Computing Center (TACC) at the University of Texas Austin. The authors thank the

Molecular Materials Research Center (MMRC) at the Beckman Institute at Caltech for use of their optical equipment for measurements performed in this work. We thank Y. Li, X. Shi and L. Chen of the Shanghai Institute of Ceramics, Chinese Academy of Sciences for ZEM-3 measurements as part of the International S&T Cooperation Program of China (2015DFA51050). We also thank H. Xiao and T. Chapasis for helpful discussions regarding this paper.

Author contributions

This paper was written collaboratively by Y.T., Z.M.G. and G.J.S. with input from all other authors. Sample synthesis, structural characterization and thermoelectric transport property measurements were performed by Y.T. Optical measurements were performed by Z.M.G. Development of the Kane band model effective mass relation was performed by Z.M.G. and confirmed by Y.T. Band modelling was done collaboratively by Y.T. and Z.M.G. with assistance from H.-S.K. Electronic band structure calculations and Fermi surface plotting were performed by L.A.A. G.L. validated L.A.A.'s DFT calculations and provided additional results and insight. M.B.N. and S.C. contributed to helpful discussions.

Additional information

Supplementary information is available in the online version of the paper. Reprints and permissions information is available online at www.nature.com/reprints. Correspondence and requests for materials should be addressed to G.J.S.

Competing financial interests

The authors declare no competing financial interests.

Methods

Sample synthesis. Samples with nominal compositions $Yb_xCo_4Sb_{12.012}$ (with x ranging from 0.0025 to 0.3) were synthesized. 0.1 at% excess of Sb was added to compensate for possible Sb evaporation. High-purity elements Co (99.95%, slug), Sb (99.9999%, shot) and Yb (99.9%, ingot) purchased from Alfa Aesar were used as raw materials. The samples were sealed in carbon-coated fused silica tubes under vacuum. The silica tubes were heated slowly up to 1,373 K in 12 h, held at this temperature for 12 h, and then quenched in water to room temperature. Samples were then annealed at 973 K for seven days. The resulting ingots were hand ground into fine powders and consolidated by rapid hot-pressing at 973 K for 1 h under a pressure of about 60 MPa, yielding fully dense bulk samples before thermoelectric property measurements.

Structure characterization. After hot-pressing, pellets were characterized by room-temperature powder X-ray diffraction (XRD), with data collected on a Panalytical X'Pert Pro diffractometer equipped with Cu Kα radiation to check phase purity and lattice parameters. Microstructures of the hot-pressed samples were checked with a Zeiss 1550VP field emission scanning electron microscope (SEM). Quantitative elemental analyses of the hot-pressed samples were performed with a JEOL JXA-8200 electron probe microanalysis (EPMA) using an accelerating voltage of 15 KeV and a current of 25 nA in a WDS mode and averaged over ten randomly selected locations in the skutterudite phase. Results from XRD, SEM and EPMA are shown in the Supplementary Information, Section 1.

Thermoelectric transport property measurements. Electrical transport properties, including electrical conductivity (σ) and Seebeck coefficient (S) were measured using the ZEM-3 (ULVAC) apparatus under a helium atmosphere from 300 to 850 K. Thermal conductivity (κ) was calculated using $\kappa = dD_T C_P$, with the thermal diffusivity D_T measured along the cross-plane direction by the laser flash method (Netzsch LFA 457) under argon flow with the Cowan model plus pulse correction. The density of the samples was measured using a geometrical method. The specific heat capacity C_P was determined using the Dulong–Petit law $C_P = 3k_B$ per atom throughout the temperature range 300 to 850 K. The in-plane Hall coefficient (R_H) was measured using the Van der Pauw method in a magnetic field up to 2 T. Hall carrier concentration (n_H) was then estimated to be equal to $1/R_H e$, where e is the elementary charge. The Hall carrier mobility (μ_n) was calculated according to the relation $\mu_n = R_H \sigma$. The estimated measurement uncertainties are listed as follows: 5% for electrical resistivity, 7% for Seebeck coefficient, 5% for thermal diffusivity and 1% for density. The data precision (reproducibility) is smaller than the accuracy, leading to zT values within the range ±0.2. Temperature-dependent transport properties are plotted in the Supplementary Information, Section 2.

Band model. In this work, a three-band transport model was used to calculate the thermoelectric properties for $CoSb_3$ at $T = 300$ and 800 K.

The properties were calculated assuming acoustic phonon scattering for all bands, with the overall properties computed using conductivity-weighted averages. The appropriate Fermi integrals were computed numerically (Python) to determine the reduced Fermi-level-dependent Seebeck, mobility, Hall coefficient, and carrier concentration. The bandgap and conduction band offset were taken from optical measurements. Additional information regarding the fitting and specific parameters is presented in the Supplementary Information, Section 4.

Owing to the large bipolar effects at high temperatures, properties were plotted against room temperature n_H from experiments. Model results were mapped to room temperature by solving the charge neutrality equation for the number of intrinsic defects at both temperatures (additional details in the Supplementary Information, Section 4).

Thermal conductivity κ was computed using a polynomial fit to give κ as a function of the room temperature carrier concentration ($n_{H,300\,K}$). These values were used to estimate zT as a function of the measured room temperature carrier concentration using different band models.

Optical measurements. Diffuse reflectance infrared Fourier transform spectroscopy (DRIFTS) measurements were performed on a Nicolet 6700 FTIR Spectrometer fitted with a Harrick Praying Mantis Diffuse Reflectance attachment and a low-temperature stage (Harrick CHC). The spectral range of the instrument was from 0.05 eV–0.8 eV. The Kubelka–Munk function, $F(R)$, was obtained from the measured diffuse reflectance (R), $F(R) = (1-R)^2/2R$, which is known to be proportional to the absorption coefficient (α) ratioed to the scattering coefficient (K).

Bandgaps were estimated using different extrapolation techniques for direct (α^2) and indirect ($\alpha^{1/2}$) transitions. First, regarding transition 1 (believed to be the direct gap, Γ–Γ transition), several extrapolation techniques were considered (hence the error bars in Fig. 3b). The direct extrapolation yielded the largest gap of around 0.23 eV (orange circles, Fig. 3b). Error bars for the direct gap were plotted indicating the actual onset of absorption (as determined through linear extrapolation to the minimum), which should give a good lower bound for the value of $E_{g,\Gamma-\Gamma}$. With increasing temperature, the estimate for the direct gap did not change much (approximately constant at 0.22 eV), although the result was obscured by free carriers for $T > 200\,°C$ (as indicated by the dashed line above these temperatures, Fig. 3b). For all temperatures with significant free carrier absorption, the free carrier absorption was fitted to a power law and subtracted from the Kubelka–Munk function to perform the absorption edge extrapolation fitting.

Transition 2 was fitted after subtracting both the free carrier absorption and the direct extrapolation (transition 1) from the spectrum. This transition was fitted as an indirect gap using either the Tauc method, $(\alpha\hbar\omega)^{1/2}$, or simply $\alpha^{1/2} \propto (\hbar\omega - (E_g \pm E_{ph}))$ (both gave similar results for the gap). This method yielded two slopes which, according to theoretical analyses, indicate the onset of phonon absorption ($-E_{ph}$) and phonon emission ($+E_{ph}$)[46]. The bandgap was extracted as either half-way between the absorption and emission intersections or simply as the emission intersection (as indicated by the symbols and error bars respectively in Fig. 3b).

The JDOS was computed numerically using the DOS (Fig. 1b, right side) as computed from DFT. The JDOS was estimated using $\mathrm{JDOS}(\hbar\omega) = \int\int \sqrt{D_{VB}(E_{VB}) D_{CB}(E_{CB})}\,\delta(E_{CB} - E_{VB} - \hbar\omega)\,dE_{vB}\,dE_{CB}$, where $D_{VB,CB}$ is the density of states of the conduction or valence band respectively and δ is the Dirac delta function (selecting only energies where the valence and conduction band energies are separated by the desired photon energy). More details about optical measurements are in the Supplementary Information, Section 3.

***Ab initio* DFT calculation and ultrafine evaluation of Fermi surfaces.** The positions of the 16 atoms in the $CoSb_3$ unit cell (with conventional lattice parameter of 9.07 Å) are relaxed using norm-conserving pseudopotentials and the Perdew–Burke–Ernzerhof (PBE; ref. 47) density functional, as implemented in the *ab initio* package Quantum Espresso[48]. The plane-wave basis set is defined by an energy cutoff of 270 Ry. Although PBE is generally known for the systematic underestimation of the bandgap of semiconductors, it can usually predict the correct topology of the bands, which is desired in this study; for such cases, the PBE electronic structure can simply be corrected by an energy shift of the unoccupied manifold via the scissor operator (details in Supplementary Information, Section 6). Previous literature also suggests that the specific bandgap value is extremely sensitive to the Sb positions and lattice parameter[20], and that the exact functional is less important. The obtained theoretical bandgap using PBE density functional agrees well with the experimental optical bandgap in this study (more details in the Supplementary Information, Section 6).

A $9 \times 9 \times 9$ Monkhorst–Pack sampling of the reciprocal space is sufficient to converge the DFT wavefunctions. However, ultrafine k-meshes are needed to obtain smooth isosurfaces ($180 \times 180 \times 180$ k-points in the reciprocal unit cell) and resolve the low-energy features of the DOS ($100 \times 100 \times 100$, with a low smearing energy of 0.02 eV). Highly accurate real-space tight-binding Hamiltonian matrices are built by projecting the DFT Bloch states onto a 'small' set of atomic orbitals (4*p*, 3*d*, 4*s* for Co; and 5*p*, 5*s* for Sb) while filtering out states of low projectability[49]. Reciprocal- and real-space Hamiltonian matrices are obtained by Fourier transformation and then diagonalized at each point of the ultrafine mesh to obtain the eigenenergies. The resulting tight-binding and the actual DFT values are numerically equivalent for all practical purposes. We used the parallel implementation of the method available in the WanT code by A. Ferretti, B. Bonferroni, A. Calzolari and M. B. Nardelli, (http://www.wannier-transport.org). XCrySDen (ref. 50) is used for visualizing the isosurfaces.

References

46. Yu, P. Y. & Cardona, M. *Fundamentals of Semiconductors* 259–264 (Springer, 1996).
47. Perdew, J. P., Burke, K. & Ernzerhof, M. Generalized gradient approximation made simple. *Phys. Rev. Lett.* **77,** 3865–3868 (1996).
48. Giannozzi, P. *et al.* QUANTUM ESPRESSO: A modular and open-source software project for quantum simulations of materials. *J. Phys. Condens. Matter* **21,** 395502 (2009).
49. Agapito, L. A., Ferretti, A., Calzolari, A., Curtarolo, S. & Buongiorno, N. M. Effective and accurate representation of extended Bloch states on finite Hilbert spaces. *Phys. Rev. B* **88,** 165127 (2013).
50. Kokalj, A. Computer graphics and graphical user interfaces as tools in simulations of matter at the atomic scale. *Comput. Mater. Sci.* **28,** 155–168 (2003).